

# SpyDir: Spy Device Localization Through Accurate Direction Finding

Wenhao Chen  
wec035@ucsd.edu  
UC San Diego  
USA

Wenyi Morty Zhang  
wez049@ucsd.edu  
UC San Diego  
USA

Wei Sun  
wei.sun@wright.edu  
Wright State University  
USA

Dinesh Bharadia  
dineshb@ucsd.edu  
UC San Diego  
USA

Roshan Ayyalasomayajula  
roshana@buffalo.edu  
University at Buffalo  
USA

arXiv:2602.00411v1 [cs.CR] 31 Jan 2026

## Abstract

Hidden spy devices (e.g., spy cameras) have become a great privacy threat recently, as these low-cost, low-power, and small form-factor IoT devices can quietly monitor human activities in the indoor environment without generating any side-channel information (e.g., wireless communication traffic and thermal noise). As such, it is difficult to detect and even more challenging to localize them in the rich-scattering indoor environment. To this end, this paper presents the design, implementation, and evaluation of SpyDir, a system that can accurately localize the hidden spy IoT devices by harnessing the electromagnetic emanations automatically and unintentionally emitted from them. Our system design mainly consists of (1) a portable switching antenna array to sniff the spectrum-spread emanations, (2) an emanation enhancement algorithm through non-coherent averaging that can de-correlate the correlated noise effect due to the square-wave emanation structure, and (3) a multipath-resolving algorithm that can exploit the relative channels using a novel optimization-based sparse AoA derivation. Our real-world experimental evaluation across different indoor environments demonstrates an average AoA error of  $6.30^\circ$ , whereas the baseline algorithm yields  $21.06^\circ$ , achieving over a  $3.3\times$  improvement in accuracy, and a mean localization error of 19.86cm over baseline algorithms of 206.79cm (MUSIC) and 294.75cm (SpotFi), achieving over a  $10.41\times$  and  $14.8\times$  improvement in accuracy.

## 1 Introduction

The rapid growth of the Internet of Things (IoT) has popularized small, low-power, and low-cost devices. However, the compact and easily deployable nature also makes IoT devices like microcameras easy to misuse for covert monitoring, which creates serious privacy risks. Recent studies show that hidden cameras are increasingly found in hotels, Airbnbs, and private homes to record indoor activities [7, 39].

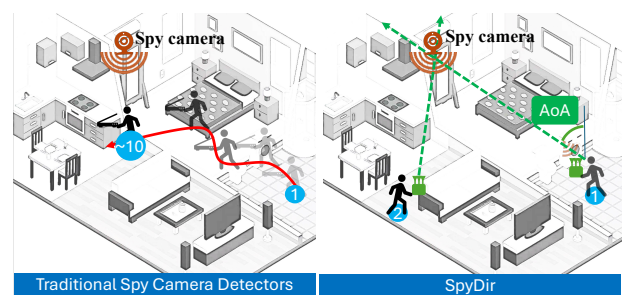


**Figure 1: SpyDir (right) can accurately locate a spy camera in just two steps, where it can sniff and derive the emanation direction through AoA estimation and further accurately localize the spy camera. Unlike traditional systems (left), which need you to scan multiple locations to detect and coarsely locate the spy camera based on the camera’s thermal noise, wireless communication traffic, or laser-based sensing, etc.**

Detecting and further localizing such covert IoT devices, particularly hidden cameras, is therefore essential for protecting user privacy.

As shown in Table 1, the prior works either lack protocol-agnostic, localization-capable, or diverse detection (i.e., different spy camera detection) properties. For example, the dedicated detectors [1, 26] or specialized sensors [14] cannot detect diverse hidden spy IoT devices. Moreover, it is difficult to detect these low-cost, low-power, and small form-factor hidden spy IoT devices, as they may not generate any side-channel information, such as wireless communication traffic and very little thermal noise, which can disable most traffic-based [4, 38], thermal imaging-based detections [49], and optical/laser sensor-based detections [10]. Recent works exploit the electromagnetic emanations [22, 40, 48] that are automatically and unintentionally emitted from the hidden cameras for detection. For example, RFScan [40] localizes hidden devices by tracing their emanation harmonics with a

Detection Model	Protocol-agnostic	Localization-capable	Diverse detection
Dedicated sensors [26]	✓	✗	✗
Traffic-based [4]	✗	✓	✗
Sensor-based (optical, laser, and thermal sensors) [10, 14, 28, 49]	✓	✗	✗
Emanation-based [45]	✓	✗	✓
<b>SpyDir</b>	✓	✓	✓

**Table 1: System property comparison of SpyDir and prior works.**

directional antenna, yet its accuracy degrades significantly in multipath-rich indoor environments. Similarly, ESauron [45] depends on the RSSI of electromagnetic radiation and suffers from parallel limitations under complex propagation conditions. CamFirm [17] induces electromagnetic responses by actively modulating ambient brightness during camera mode switching for localization. However, this approach only functions reliably in relatively dim lighting, which restricts its practical applicability in typical indoor scenarios. Therefore, localizing hidden cameras from their unintentional emanations in complex real-world environments remains an open challenge, due to strong multipath effects and the inherently low signal-to-noise ratio of these emanations. Considering these constraints in realistic indoor scenarios, we identify and address three key challenges that hinder accurate localization:

(1) *A portable and low-cost array for emanation eavesdropping.* Hidden cameras emit amplitude-modulated clock signals whose emanation spikes appear across a wide and discontinuous sub-GHz spectrum. Accurately localizing these devices requires capturing these distributed spikes while retaining the spatial resolution needed for Angle-of-Arrival (AoA) estimation. A conventional solution is to use a bulky multi-antenna array with multiple RF chains, but such setups are expensive and impractical. To make localization feasible with low-cost and readily available hardware, *we design a handheld switching-antenna array PCB that uses only a synchronized dual-channel RF front-end (e.g., a standard USRP).* This design remains compact and inexpensive while still achieving the high-speed switching necessary to derive the relative channels used for emanation-based AoA estimation and localization.

(2) *Emanation enhancement, noise decoupling, and interference detection.* Unintentional clock emanations from hidden cameras are inherently very weak, making their spectral spikes difficult to detect and even harder to use for localization. Non-coherent averaging would ideally boost the signal strength. However, in a switching-antenna architecture, we observed in practice that the noise introduced at different antenna positions is correlated, preventing effective signal enhancement. To address this, we adapt non-coherent averaging by introducing controlled delays that leverage the

periodic square-wave structure of the emanations. *These delays drive the noise components out of phase and reduce their correlation, while the structured emanation remains consistently reinforced.* As a result, the switching noise is mitigated, and the effective emanation energy is boosted.

(3) *AoA estimation with sparse and joint optimization.* Indoor environments introduce strong multipath that significantly distorts the phase of the received emanations, making localization difficult in cluttered spaces. Although a switched antenna array can, in principle, estimate AoA through triangulation, unintentional emanations do not contain pilots, so conventional CSI (Channel State Information)-based approaches, such as MUSIC [34], cannot be applied. Inspired by SpotFi [12], we extract relative channels by comparing each switched antenna element with a fixed reference antenna. However, the resulting smoothed relative CSI matrix has limited rank, which prevents effective separation of multiple paths. To address this limitation, *we propose a sparse optimization algorithm that recovers multiple AoAs more reliably than SpotFi-style smoothing.* Specifically, we construct multiple overlapping subspaces to artificially increase the rank and improve multipath resolvability, which can partially compensate for the limitation introduced by the relative-channel structure.

In this paper, we propose SpyDir, a system that accurately localizes hidden cameras by estimating the AoA of their automatic and unintentional emanations using a portable switching-antenna array, as shown in Fig. 1. SpyDir monitors the spectrum-spread electromagnetic emanations from *diverse spy cameras w/ or w/o wireless communication architectures*, performs *protocol-agnostic* spectrum analysis, and remains robust under strong indoor multipath, enabling accurate *localization* through a novel noise decorrelation approach and an innovative sparse optimization algorithm. As such, our SpyDir achieves the protocol-agnostic, localization-capable, and diverse devices sensing properties as shown in Table 1.

We implement SpyDir using software-defined radios (USRPs) and a custom high-speed switching-antenna PCB, and evaluate it across diverse indoor environments and multiple representative hidden-camera devices. Our evaluation spans multiple hidden-camera devices, diverse indoor environments, varying distances and frequencies, and different

packet volumes, together with analyses of algorithmic variants and parameter choices. Overall, SpyDir achieves an average AoA error of  $6.30^\circ$ , offering over a  $3.3\times$  improvement relative to MUSIC. When deployed for full 2D localization, SpyDir attains an average position error of 19.86 cm, whereas MUSIC and SpotFi exceed 200 cm and 290 cm, respectively—corresponding to  $10\times$ – $15\times$  localization accuracy improvement in real indoor environments. Our contributions are listed as follows:

- To the best of our knowledge, we present the first system that accurately localizes hidden spy IoT devices using unintentional emanations in multipath-rich indoor environments.
- We design a compact wideband switched-antenna array and signal-enhancement pipeline that boosts extremely weak emanations by combining non-coherent averaging with a novel noise decorrelation approach.
- We develop a sparse optimization algorithm that derives reliable AoA estimates from relative CSI obtained through antenna switching, which is not possible with the state-of-the-art AoA estimation algorithms.
- We validate SpyDir across diverse indoor settings, device types, and operating conditions, demonstrating its practicality and significantly improved AoA accuracy compared to existing baselines. We also plan to open-source our implementation and hardware design to facilitate reproducibility and future research.

## 2 Background

We begin by briefly describing how leakage signals behave and how existing state-of-the-art detection algorithms identify spy devices. These primers clarify the capabilities and limitations of current systems, which focus on detecting such devices but not locating them. We then present in section 4 how SpyDir enables practical localization of spy devices in real-world deployments.

### 2.1 Understanding Leakage Signals

**Physical principle.** Hidden spy IoT devices, such as hidden spy cameras, contain CPUs and memory modules driven by internal clock signals. These clock signals, when coupled with computational activities like memory access, produce amplitude-modulated clock signals commonly referred to as electromagnetic emanations or emanations. Although unintentional, these emanations automatically leak through circuit traces, interconnects, and communication lines on the device, which effectively behave as small radio-frequency antennas. As a result, hidden cameras emit detectable RF leakage signals without any modification to their hardware or firmware.

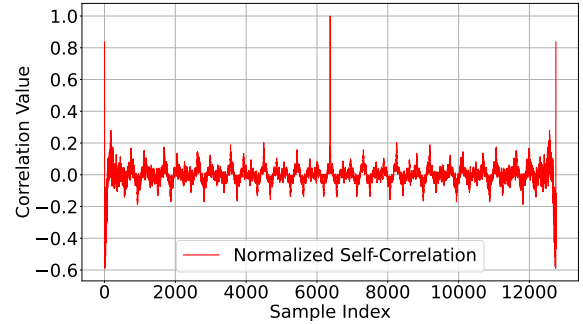


**Figure 2: Autocorrelation of an emanation signal showing clear harmonics of the device’s internal clock.**

**Emanation characteristics.** In the time domain, the emanations appear as square-wave patterns because the internal clock is amplitude-modulated by the device’s computational activity. In the frequency domain, these signals spread across a wide sub-GHz band and produce multiple harmonics/spikes, including the fundamental frequency and its higher-order multiples. Due to this spectral spreading, the harmonic components are weak, and their strength decreases with frequency. The spacing between adjacent harmonics reflects the underlying clock frequency, which can be identified through the autocorrelation of the received IQ samples. As shown in Fig. 2, the autocorrelation exhibits periodic peaks corresponding to the clock frequency, enabling both emanation detection and subsequent localization.

### 2.2 Limitations of Existing Leakage Detection

To detect emanations, the goal is to identify the amplitude-modulated clock signals, which appear as square waves in the time domain and as harmonics or spikes in the frequency domain. Previous work [22, 37, 40, 48] typically detects these harmonics by first applying a Fourier transform and then locating the spectral spikes corresponding to the device’s clock frequency. Accurate clock-frequency estimation requires identifying all harmonics across a wide frequency band. However, higher-order harmonics are often much weaker, and emanations in general have inherently low power. As a result, existing systems often rely on directional antennas, power amplification, or extensive spectral averaging to boost these weak spikes before detection. Once the emanation spikes are detected and the clock frequency is derived, the presence of concealed spy devices within the scene can be confirmed.

However, these approaches focus exclusively on detection rather than localization, and they depend on hardware or averaging techniques that do not generalize well to practical AoA estimation under weak unintentional signals, strong

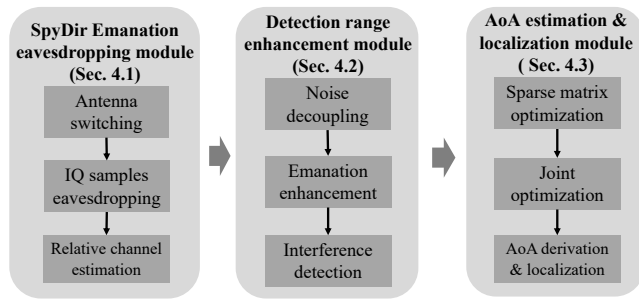


Figure 3: The workflow of SpyDir consists of three modules: the switched-antenna array module, the detection enhancement module, and the AoA estimation and localization module.

multi-path, and low SNR in real indoor environments. Addressing these limitations requires a fundamentally different design. In this paper, we tackle both the weak-signal problem and the challenge of estimating the blind source signal AoA for localization, and develop SpyDir, which is described in the next section.

### 3 System Overview

Fig. 3 shows the workflow of SpyDir, which consists of three modules: 1) the SpyDir emanation eavesdropping module, 2) the detection enhancement module, and 3) the AoA estimation and localization module. During localization, the switched-antenna array passively captures emanation signals from hidden spy devices in the indoor environment, and our algorithms process these signals to determine the device’s exact location. We summarize the function of each module below:

- **SpyDir emanation eavesdropping module (§4.1).** To analyze the emanations emitted from the spy cameras, we leverage a compact switched-antenna array that uses only two RF ports, allowing direct use with commodity USRPs while still enabling estimation of the relative channels between the reference antenna and each antenna element. As such, our SpyDir is portable for ubiquitous spy camera localization in any indoor environment.
- **Detection enhancement module (§4.2).** Using the estimated channels, we enhance the weak emanation signals through non-coherent averaging and a delay-based noise decorrelation technique, extending the effective detection range to up to 3.6 m while maintaining an AoA error below  $20^\circ$ . Moreover, we also detect the diverse ambient emanation interferences and further eliminate them for accurate relative channel estimation.
- **AoA estimation and localization module (§4.3).** With enhanced relative channels, we apply a sparse matrix optimization algorithm, including a sparse optimization and a

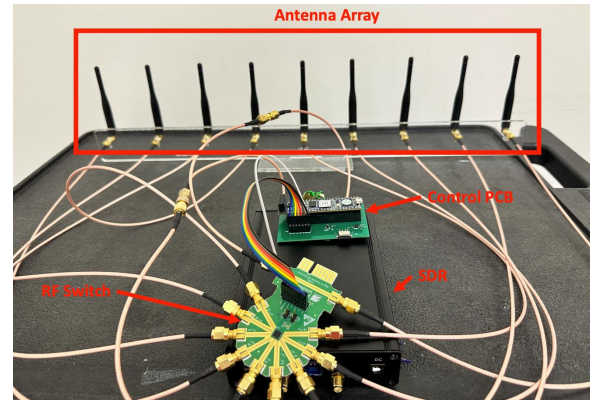


Figure 4: SpyDir consists of the RF switch, SDR, control PCB, and an antenna array.

joint optimization, to accurately estimate the AoA of the emanations and localize the hidden camera.

## 4 System Design

### 4.1 SpyDir Emanation Eavesdropping

As described in §2.2, detecting emanations simply involves identifying the repetitive harmonics in the frequency domain that arise from the device’s square-wave clock. In contrast, estimating the angle of arrival (AoA) is significantly more challenging, as it requires coherent phase information across antennas and samples. This corresponds to a blind-source estimation problem, where the transmitted waveform is unknown [23, 44]. To address this, we want to leverage a portable mobile device that can eavesdrop on the emanations from the spy camera.

**Primer on Switched-Antenna Array.** To do so, we leverage a switched-reference antenna array in which one antenna serves as a fixed reference while the remaining antennas are connected to a high-speed RF switch, as shown in Fig. 4. Then, we can switch to different antennas while maintaining only two RF ports, which enables us to use a two-port software-defined radio (SDR) for emanation eavesdropping. The wireless signals received across the switched antennas can be used to emulate an antenna-array-based signal processing. Since it only requires two RF chains for signal processing, we can use a simple and portable SDR (e.g., USRP B210) for emanation signal processing and emanation source localization.

**Leverage Switched-Antenna Array for Emanation Eavesdropping.** Our implementation uses both RX ports of a USRP B210 operating in synchronized mode: one RF port is directly connected to the reference antenna, and the other is connected to the RF switch, which sequentially selects among the array elements. This design requires only one inexpensive

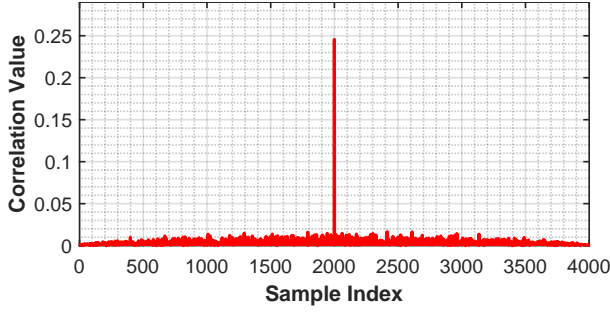


**Figure 5: Noise cross-correlation between the switched antenna and the reference antenna, measured in an anechoic chamber. With no external signals present, the received samples contain only hardware and environmental noise, revealing strong noise correlation across antennas.**

USRP with two RX ports, instead of multi-channel or multi-USRP synchronized systems typically required for coherent arrays. The internal 40 kHz clock of the B210 is tapped and used to generate synchronized control signals for the switch, ensuring precise alignment between the USRP sampling and the antenna-switching cycle.

Unfortunately, leakage signals rarely satisfy these conditions in our real-world observations. *In practice, the SNR is low, especially as the distance to the spy device increases, and the noise components across the reference and switched antennas are not independent.* To address this, SpyDir explicitly models the noise coupling and introduces a phase-offset-based relative channel estimator, which decorrelates the noise components and significantly extends the effective leakage-signal detection range (by more than 100%), as discussed in the next section.

## 4.2 Enhancing Detection Range

**4.2.1 Relative Channel Estimation Paradigm.** In switched-antenna array systems, the device does not measure the CSI directly. Instead, it obtains the relative channel by computing the phase and amplitude shift between the reference antenna and each switched antenna. Let  $r_{\text{ref}}(t)$  denote the received signal at the reference antenna. For the  $i$ th antenna in an  $N_{\text{ant}}$ -element switched array ( $i \in \{1, 2, \dots, N_{\text{ant}}\}$ ), let  $r_{i,\text{switch}}(t)$  be its received signal. A widely used estimator for extracting the relative narrowband channel is:

$$h_i^{\text{est}} = \frac{\mathbb{E}[r_{i,\text{switch}}(t)r_{\text{ref}}^*(t)]}{\mathbb{E}[|r_{\text{ref}}(t)|^2]}. \quad (1)$$

where  $h_i^{\text{est}}$  represents the estimated relative channel of the  $i$ th antenna.  $\mathbb{E}[\cdot]$  is the expectation operator over time. For narrow-band signals the received samples can be further

expressed in terms of signal and noise as follows:

$$r_{i,\text{switch}}(t) = h_i s(t) + n_i(t), \quad r_{\text{ref}}(t) = s(t) + n_{\text{ref}}(t) \quad (2)$$

where  $h_i$ ,  $s(t)$ , and  $n_i(t)$  denote the true relative channel, the target signal, and the noise at the  $i$ th switch antenna, respectively. Substituting the signal and noise components into Eq. (1), we obtain:

$$\begin{aligned} h_i^{\text{est}} &= \frac{\mathbb{E}[(h_i s(t) + n_i(t))(s^*(t) + n_{\text{ref}}^*(t))]}{\mathbb{E}[(s(t) + n_{\text{ref}}(t))(s^*(t) + n_{\text{ref}}^*(t))]} \\ &= \frac{h_i S(0) + h_i C_{\text{ref}}(0) + C_i^*(0) + N_{i,\text{ref}}(0)}{S(0) + C_{\text{ref}}(0) + C_{\text{ref}}^*(0) + N_{\text{ref},\text{ref}}(0)} \end{aligned} \quad (3)$$

where  $S(\tau) = \mathbb{E}[s(t)s^*(t - \tau)]$  is the autocorrelation matrix for the signal ( $s(t)$ ),  $C_i(\tau) = \mathbb{E}[s(t)n_i^*(t - \tau)]$  is the cross-correlation between the signal and noise measured at the  $i$ th antenna ( $n_i(t)$ ), and  $N_{i,k}(\tau) = \mathbb{E}[n_i(t)n_k^*(t - \tau)]$  is the cross correlation between the noise components of the measurements at  $i$ th and  $k$ th antenna. Now looking at Eq 3 we can see that only when the SNR is high and the noise across reference and switch antenna are independent,  $h_i^{\text{est}}$  reduces to  $h_i$ , which is the true relative channel we wanted to measure<sup>1</sup>.

**4.2.2 Noise Coupling in Low SNR Scenarios.** However, as discussed earlier, achieving high SNR is difficult in our setting because clock-leakage signals inherently carry very little energy. In addition, we observe that unavoidable factors such as antenna coupling and shared hardware paths cause the noise received at different antennas to exhibit strong correlation, as shown in Fig. 5. Although the clock signal approximates a square wave in the time domain (yielding  $C(\tau) \approx \mathbb{E}[N(t - \tau)] \rightarrow 0$ , allowing  $C(0)$  to be ignored), the strong cross-antenna noise correlation remains problematic. This correlation produces a biased estimator for  $h_i^{\text{est}}$ , as derived in Eq. 4:

$$\begin{aligned} h_i^{\text{est}} &= \frac{h_i S(0) + N_{i,\text{ref}}(0)}{S(0) + N_{\text{ref},\text{ref}}(0)} \\ &= h_i \frac{S(0)}{S(0) + N_{\text{ref},\text{ref}}(0)} + \frac{N_{i,\text{ref}}(0)}{S(0) + N_{\text{ref},\text{ref}}(0)} \end{aligned} \quad (4)$$

The resulting bias increases as the SNR decreases, making accurate channel estimation more difficult in low-SNR conditions.

**4.2.3 SNR Enhancement.** The most common method for improving SNR is coherent averaging [43], which requires collecting a large number of phase-aligned packets and averaging them. However, synchronizing the initial phase of a

<sup>1</sup>In this case,  $C(0)$  and  $N(0)$  can be ignored, with  $S(0)$  being the dominant term.

low-energy and unknown waveform across packets is extremely difficult. The limited coherence time of the channel further restricts the applicability of this technique.

In this section, we propose a time-offset estimator that significantly enhances SNR without increasing the number of received samples. We observe that the clock-leakage signal has a nearly constant period, which leads to strong periodic autocorrelation. In contrast, the cross-correlation of noise closely resembles a unit impulse,  $\delta(t)$ . By exploiting these properties, we introduce a carefully chosen time offset into the standard estimator:

$$\begin{aligned} h_{i,\tau}^{\text{offset}} &= \frac{\mathbb{E}[r_{i,\text{switch}}(t)r_{\text{ref}}^*(t-\tau)]}{\mathbb{E}[r_{\text{ref}}(t)r_{\text{ref}}^*(t-\tau)]} \\ &= \frac{h_i S(\tau) + h_i C_{\text{ref}}(\tau) + C_i^*(\tau) + N_{i,\text{ref}}(\tau)}{S(\tau) + C_{\text{ref}}(\tau) + C_{\text{ref}}^*(\tau) + N_{\text{ref},\text{ref}}(\tau)} \end{aligned} \quad (5)$$

As discussed earlier, because the clock-leakage signal closely approximates a square wave, the term  $C(\tau)$  can be treated as negligible. Substituting this approximation into the estimator, we can get:

$$h_{i,\tau}^{\text{offset}} = h_i \frac{S(\tau)}{S(\tau) + N_{\text{ref},\text{ref}}(\tau)} + \frac{N_{i,\text{ref}}(\tau)}{S(\tau) + N_{\text{ref},\text{ref}}(\tau)} \quad (6)$$

In this case, the effective SNR becomes  $\frac{S(\tau)}{N(\tau)}$ . By selecting an appropriate value of  $\tau$ , we can theoretically increase the SNR indefinitely. As discussed before, the autocorrelation and cross-correlation of noise approximate a unit-impulse function,  $\delta(t)$ , while the target signal exhibits strong periodic autocorrelation properties. In fact, choosing  $\tau$  as an integer multiple of the target signal's period often yields good results. Consequently, selecting  $\tau$  as an integer multiple of the signal period often yields favorable results.

**4.2.4 Interference Detection.** Clock leakage occurs at specific frequencies that often coincide with emissions from other electronic devices. As a result, interference is unavoidable in realistic indoor environments. In this section, we analyze how interference affects our estimator and describe how SpyDir detects the presence of interference.

Let the target leakage signal be  $s(t)$  and an interfering leakage signal be  $d(t)$ . The signal received at the reference antenna is:

$$r_{\text{ref}}(t) = s(t) + d(t),$$

and the signal received at the  $i$ -th switched antenna is:

$$r_i(t) = h_i s(t) + \alpha_i d(t),$$

where  $h_i$  and  $\alpha_i$  denote the channels of the target and interference signals, respectively. For clarity, we omit noise

terms and focus on how interference interacts with our SNR-enhancement estimator. The estimated channel becomes:

$$\begin{aligned} h_{i,\tau}^{\text{offset}} &= h_i \frac{S(\tau) + C(\tau)}{S(\tau) + C(\tau) + C^*(-\tau) + D(\tau)} \\ &\quad + \alpha_i \frac{C^*(-\tau) + D(\tau)}{S(\tau) + C(\tau) + C^*(-\tau) + D(\tau)} \end{aligned} \quad (7)$$

where  $C(\tau) = \mathbb{E}[s(t)d^*(t-\tau)]$ . As shown in the equation above, interference simply adds additional channel components, each scaled by a normalized weight. In other words, interference only introduces extra AoA paths rather than corrupting or destroying the true target direction. Based on this observation, SpyDir detects the presence of interference by also computing the inverse-offset estimate  $h_{i,\tau}^{\text{inverse}}$  from Eq. 8 and comparing it with the expression in Eq. 7:

$$\begin{aligned} h_{i,\tau}^{\text{inverse}} &= \frac{\mathbb{E}[r_{i,\text{switch}}(t-\tau)r_{\text{ref}}^*(t)]}{\mathbb{E}[r_{\text{ref}}(t-\tau)r_{\text{ref}}^*(t)]} \\ &= h_i \frac{S^*(\tau) + C(-\tau)}{S^*(\tau) + C^*(\tau) + C(-\tau) + D^*(\tau)} \\ &\quad + \alpha_i \frac{C^*(\tau) + D^*(\tau)}{S^*(\tau) + C^*(\tau) + C(-\tau) + D^*(\tau)} \end{aligned} \quad (8)$$

In the absence of interference, both Eq. 7 and Eq. 8 reduce to  $h_{i,\tau}^{\text{offset}} = h_{i,\tau}^{\text{inverse}} = h_i$ . Therefore, any deviation between  $h_{i,\tau}^{\text{offset}}$  and  $h_{i,\tau}^{\text{inverse}}$  indicates the presence of interference. In such cases, we can re-estimate the channel using samples from a different time segment. This mechanism makes SpyDir robust to environmental interference and enables it to detect and localize devices whose leakage signals may otherwise be masked by stronger emissions.

### 4.3 Estimate Accurate AoA

Using the proposed estimator, the recovered channel reflects the ratio between the true channels of the switched antenna and the reference antenna. In the presence of multipath, the relative channel observed at the  $i$ -th switched antenna can be expressed as:

$$h_i = \frac{\sum_{k=1}^m w_k e^{-j2\pi \sin(\theta_k) d/\lambda}}{\sum_{k=1}^m w_k} \quad (9)$$

where  $m$  denotes the number of propagation paths,  $w_k$  is the complex gain of the  $k$ -th path at the reference antenna,  $\theta_k$  is its angle of arrival (AoA),  $d$  is the antenna spacing, and  $\lambda$  is the signal wavelength. By switching across all  $N$  antennas, we obtain the relative channel vector:

$$\frac{1}{\sum_{k=1}^m w_k} \left[ \sum_{k=1}^m w_k, \sum_{k=1}^m w_k \phi_k, \sum_{k=1}^m w_k \phi_k^2, \dots, \sum_{k=1}^m w_k \phi_k^N \right] \quad (10)$$

where  $\phi_k = e^{-j2\pi \sin(\theta_k) d/\lambda}$  is the per-antenna phase shift of the  $k$ -th path induced by the array geometry.

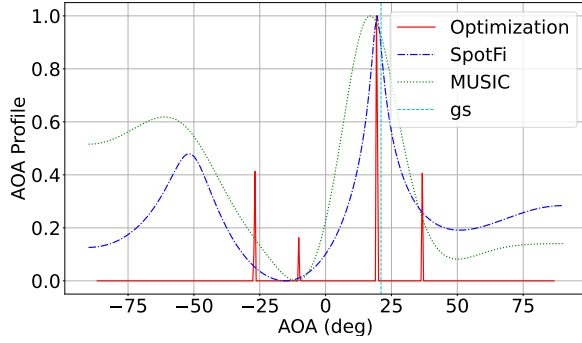


**Figure 6: SpyDir ’s AoA estimator (labeled “Optimization”) provides significantly higher angular resolution than existing super-resolution methods such as MUSIC [34] and SpotFi [12]. “gs” denotes the ground-truth direction.**

**4.3.1 Limitations of SpotFi/MUSIC-Based AoA Estimation.** Directly applying the relative channel vector in Eq. 10 to the MUSIC algorithm produces a signal subspace with rank = 1. This occurs because all antennas observe the same set of multipath components up to a common normalization term. As a result, multipath cannot be effectively separated, and the AoA estimates degrade severely.

To mitigate this, we consider a SpotFi-inspired approach that constructs multiple overlapping subspaces to artificially increase rank and improve multipath resolvability. This technique trades off the number of usable antennas in order to generate a set of short, full-rank channel segments.

For instance, in a system with 9 antennas (8 switched elements and 1 reference), we can select every 5 consecutive channel values to form a subspace, yielding a  $5 \times 5$  covariance matrix with full rank. This improves the ability to resolve multiple propagation paths and partially compensates for the limitations imposed by the relative-channel structure.

**4.3.2 Sparse Matrix Optimization.** To overcome the low-rank limitations of the estimated channel matrix, which fundamentally restrict the performance of super-resolution algorithms such as MUSIC and SpotFi, we formulate a sparse representation of the AoA profile and solve it using a sparse-matrix optimization procedure. This enables high-resolution AoA estimation, as illustrated in Fig. 6.

**IFFT and Window Effects.** A classical alternative for obtaining an AoA profile is to apply an inverse fast Fourier transform (IFFT), which maps the antenna domain into the spatial (AoA) domain [3]. Applying a large-size IFFT to the channel vector in Eq. 10 yields:

$$P(\Psi) = \sum_{k=1}^m \left( \frac{w_k}{\sum_{k=1}^m w_k} \delta \left( \Psi - \frac{d \sin(\theta_k)}{\lambda} \right) \right) * w_{\text{sinc}}(\Psi) \quad (11)$$

where  $*$  denotes convolution and  $w_{\text{sinc}}(\Psi)$  is the sinc-shaped window function imposed by the finite number of antennas. The width of this window directly limits the resolution of any IFFT-based AoA estimate.

Since the IFFT result is discrete, the convolution can be equivalently rewritten in matrix form as  $\vec{P} = \vec{W}\vec{a}$  where  $\vec{P}$  is a  $D \times 1$  vector (IFFT result with FFT size  $D$ ),  $\vec{W}$  is a  $D \times D$  window matrix whose columns are shifted versions of  $w_{\text{sinc}}(\Psi)$  and  $\vec{a}$  is a  $D \times 1$  sparse vector encoding the underlying AoA components.

A natural approach for estimating  $\vec{a}$  is to solve the least-squares problem:

$$\min_{\vec{a}} \|\vec{P} - \vec{W}\vec{a}\|_2 \quad (12)$$

However, because the rank of the window matrix  $\vec{W}$  is fundamentally limited by the number of antennas, the optimization in Eq. 12 becomes undetermined.

**Sparse Optimization.** To resolve the undetermined system caused by the limited rank of  $\vec{W}$ , we incorporate structural constraints on the AoA profile. From the IFFT formulation, the true AoA representation can be written as:

$$\vec{a} = \sum_{k=1}^m \frac{w_k}{\sum_{k=1}^m w_k} \delta \left( \Psi - \frac{d \sin(\theta_k)}{\lambda} \right)$$

which reveals several important properties. First,  $\vec{a}$  is sparse: it contains only  $m$  nonzero entries corresponding to the  $m$  propagation paths. Second, the nonzero entries sum to one due to the normalization term. Third, the support of  $\vec{a}$  is restricted to the physically valid region:

$$|\Psi| = \left| \frac{d \sin(\theta)}{\lambda} \right| \leq \frac{d}{\lambda},$$

because  $|\sin(\theta)| \leq 1$ . Thus, when the antenna spacing satisfies  $d < \frac{\lambda}{2}$ , all entries of  $\vec{a}$  outside the interval  $[-d/\lambda, d/\lambda]$  must be zero, further reducing the feasible search space.

Leveraging these observations, we impose sparsity and support constraints on  $\vec{a}$  and obtain the following constrained optimization formulation for AoA estimation:

$$\begin{aligned} \min_{\vec{a}} \quad & \|\vec{P} - \vec{W}\vec{a}\|_2 + \beta \|\vec{a}\|_1 \\ \text{s.t.} \quad & \sum \vec{a} = 1 \\ & \vec{a}(\Psi) = 0, \quad \forall |\Psi| > \frac{d}{\lambda} \end{aligned} \quad (13)$$

where we introduce the  $\ell_1$ -norm of  $\vec{a}$ ,  $\|\vec{a}\|_1$ , to approximate the  $\ell_0$ -norm and ensure a sparse solution, which constraints further tighten the solution. Thus, using this sparse-matrix representation and the constrained optimization formulated in Eq. 13, we enhance the AoA estimation resolution even for the low-ranked leakage signal measurements across SpyDir’s antenna array. Thus enabling accurate direction finding of the Spy Device in any given indoor environment, not only

to detect but to identify for accurate position of where the Spy device is within the environment.

**Joint Optimization.** To improve the accuracy of angle-of-arrival (AoA) estimation in a given spatial scenario, we exploit multiple channel measurements obtained under different dimensions, such as frequency, time, or deliberately introduced offsets. Suppose we have  $L$  such measurements, each providing an IFFT-based spatial profile denoted as  $P_i$ .

For each measurement, the conventional sparse formulation seeks an AoA profile  $a_i$  via:

$$\min_{a_i} \|P_i - W_i a_i\|_2^2 + \beta \|a_i\|_1,$$

where  $W_i$  is the dictionary of window functions of  $i^{\text{th}}$  measurement. However, to enforce consistency across measurements—i.e., that they share the same underlying set of active angles—we adopt a joint optimization framework. We stack all sparse codes as columns of a matrix:

$$A = [a_1, a_2, \dots, a_L],$$

and formulate the following group-sparse objective:

$$\min_A \sum_{i=1}^L \|P_i - W_i a_i\|_2^2 + \lambda \sum_{j=1}^M \|A_{j,:}\|_2,$$

where  $M$  is the number of candidate angles. The mixed-norm regularization term  $\sum_j \|A_{j,:}\|_2$  promotes *row-wise group sparsity* in  $A$ , ensuring that entire rows are either all zeros or all non-zeros across samples. This induces a shared support set of active angles, thereby improving estimation robustness under diverse channel conditions. In addition, since those measurements are independent, the constraints of the joint optimization problem are simply the superposition of constraints of each sub-problem.

**Additional Benefits of Joint Optimization.** Beyond improving AoA accuracy through shared-support recovery, our joint optimization framework also enables cross-dimensional analysis of the channel. As noted earlier, the non-zero entries in the recovered AoA profiles are proportional to

$$\frac{w_k}{\sum_{k=1}^m w_k}$$

which correspond to the relative channel gain of each propagation path. Tracking how these non-zero coefficients vary across the  $L$  measurements, therefore, provides additional insights into the propagation environment:

- *Temporal diversity:* When measurements are collected at different time instants, variations in the coefficients at a given AoA reflect the temporal evolution of each propagation path, enabling the tracking of slow fading or device mobility.
- *Frequency diversity:* When measurements span multiple frequencies, the coefficient variations encode the underlying path delays, since frequency-dependent phase shifts

correspond to time-difference-of-arrival (TDOA) information.

- *Offset diversity:* When deliberate time offsets are applied during measurement, differences in coefficient behavior help distinguish interfering signals that exhibit different autocorrelation structures.

Together, the joint framework not only enforces a consistent set of active angles across all measurements, but also provides a principled way to characterize how propagation paths evolve across time, frequency, and offset dimensions.

## 5 Implementation and Setup

**Hardware and Software.** Our hardware platform consists of a switched antenna array controlled by a custom PCB for high-speed switching during emanation signal collection. The antenna array is built using commercial off-the-shelf (COTS) antennas and a PE42582 SP8T RF switch evaluation board [27], which supports an operational frequency range of 9 kHz-8 GHz. This allows fast switching within the coherence time of the emanation signal, driven by external control logic that toggles among the antenna ports. The evaluation board provides eight RF input ports connected to the antennas and one RF common port connected to a USRP B210 receive chain. All antennas are mounted on laser-cut acrylic plates supporting up to eight elements in any configuration. The calibration trace on the evaluation board routes one end to the reference antenna and the other to the B210's second receive chain, enabling simultaneous reference IQ capture for signal identification.

We design a custom PCB to control the RF switch and supply the required bias voltages. On-board LDOs generate a 3.4V supply ( $V_{DD}$ ) and a -3V bias voltage for rapid switching. A CMOD A7-35T FPGA handles antenna-port selection. The FPGA implements a finite-state machine (FSM) clocked at 40 MHz and synchronized using trigger and reset signals from the USRP B210.

The control logic ensures that none of the eight input ports is connected to the common port while the system is idle. When the reset signal is logic low, the FSM waits for a trigger pulse to begin the switching sequence. Upon receiving the trigger, the FSM cycles through antennas by asserting a 3-bit control signal (V1-V3) corresponding to the selected input port. The switching period is determined by a configurable parameter, *switch\_time*, which is sent from a Python interface to the FPGA via UART before each measurement run. During each *switch\_time* interval, the 3-bit control signal increments by one, selecting the next antenna in sequence. When the reset line is asserted high, the FSM halts and returns to its initial state. Our signal processing algorithms are mainly implemented in Python.

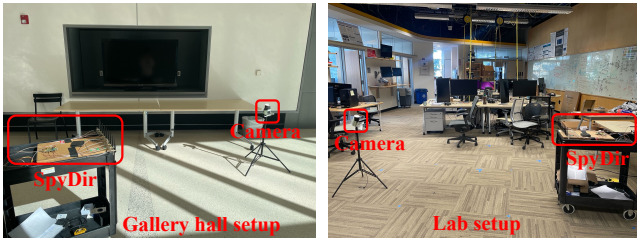


**Figure 7: Real-world experimental evaluation of SpyDir’s switched-antenna receiver for hidden spy camera AoA estimation in the gallery hall and lab.**

**Experimental settings.** Both USRP RX ports operate at a 3.072MS/s sample rate with a receive gain of 75 dB. A uniform linear array (ULA) of eight switched antennas is used, with an inter-element spacing of 62.5mm to balance array size and frequency-dependent mismatch. The RF switch cycles through all eight antennas within a total switching interval of  $31.25 \text{ ms} \times 8$ . A Linux machine equipped with an Intel i7-1185G7 CPU running Ubuntu 20.04 drives the USRP and performs subsequent signal processing using Python-based implementations.

We deploy SpyDir in indoor environments with strong multipath. The hidden cameras are placed at distances between 2-4m from the SpyDir setup. For each measurement run, we collect 50s of IQ samples from the emanations unintentionally emitted by the spy devices. From these samples, we identify emanation harmonics spread over the 1GHz sub-GHz band, which are then used for AoA estimation.

We evaluate SpyDir using two representative commercial spy-camera devices (OV2640 [30] and HZVS4730 [8]) that do not actively transmit RF signals but nonetheless emit continuous electromagnetic leakage. Experiments are conducted in multipath-rich and non-line-of-sight (NLoS) scenarios, including deployment behind walls, as illustrated in Fig. 7. We compare our AoA estimation performance against state-of-the-art methods, including SpotFi [12] and the MUSIC algorithm [9].

## 6 Evaluation

We evaluate SpyDir across three dimensions: (1) a real-world 2D localization case study comparing triangulated results with baselines; (2) end-to-end AoA accuracy benchmarking across algorithms, device types, and averaging strategies; (3) targeted microbenchmarks evaluating the effects of range, time-offset noise decorrelation, time-averaging window size, and sparsity parameter  $\beta$  on AoA performance. We mainly report the localization error, AoA estimation error, and the emanation SNR. All experiments use the hardware and deployment setup described in §5.

**Table 2: Localization error across five target locations.**

Location	SpyDir (cm)	MUSIC (cm)	SpotFi (cm)
1	<b>46.01</b>	320.16	408.77
2	<b>5.39</b>	170.58	249.66
3	<b>17.46</b>	171.17	281.47
4	<b>11.18</b>	201.82	275.09
5	<b>22.36</b>	166.21	256.77
<b>Avg.</b>	<b>19.86</b>	206.79	294.75

### 6.1 Case Study: 2D Localization

We demonstrate how SpyDir can be deployed in a real-world indoor environment to locate a hidden spy camera.

**Method:** We place the spy camera at five different locations within a  $5 \text{ m} \times 5 \text{ m}$  lab space containing numerous electronic devices and IoT equipment, all of which serve as strong sources of interference. SpyDir identifies the target device by leveraging its unique clock frequency and the self-correlation-based interference detection mechanism described in section 4.2.4.

To obtain multiple vantage points for triangulation, we position SpyDir’s switched-antenna receiver at five different locations throughout the lab. At each vantage point, we collect leakage measurements and estimate the AoA of the spy camera. The final 2D position estimate is obtained by triangulating these AoA results.

**Results:** Fig. 8(a–e) shows the triangulation performance across five target locations. Table 2 reports the localization error for the five target locations. SpyDir achieves an average error of 19.86 cm, with individual errors ranging from 5.39 cm to 46.01 cm. In four of the five cases, the error remains within 5–25 cm, demonstrating stable high accuracy even under strong interference from surrounding IoT devices. The localization error of 46.01 cm is mainly because the spy camera is at the edge of the aperture range of the switched-antenna array, resulting in noisy emanations.

In contrast, MUSIC and SpotFi perform substantially worse, with average errors of 206.79 cm and 294.75 cm, respectively. Aggregating across all deployments, SpyDir improves localization accuracy by  $10.4\times$  over MUSIC and  $14.8\times$  over SpotFi, highlighting that classical AoA algorithms cannot reliably operate on weak, unintentional emanations, whereas SpyDir’s sparse optimization and noise-decorrelation pipeline successfully recovers fine-grained directional information.

### 6.2 End-to-End AoA Performance

To comprehensively evaluate the AoA estimation performance of our proposed system, we conduct extensive experiments under diverse multipath-rich indoor environments. Our evaluation focuses on three key aspects:

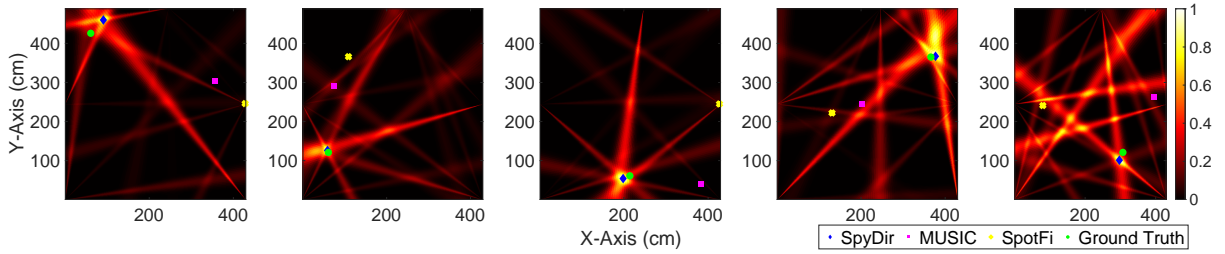
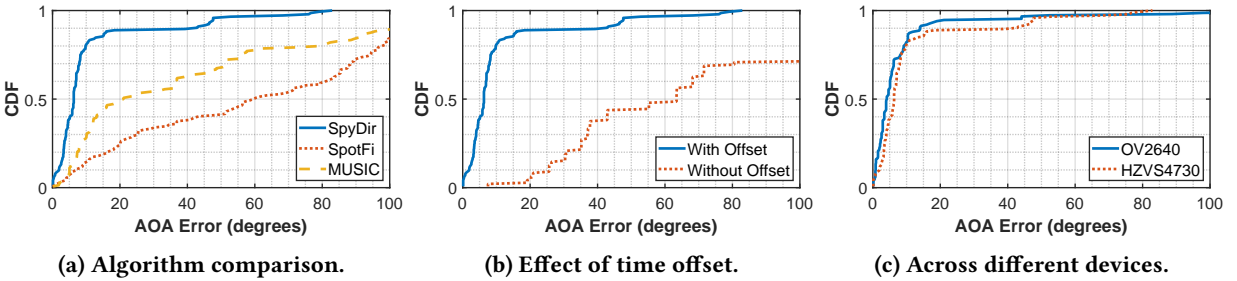


**Figure 8: Ground Truth and the Triangulated 2D location results using SpyDir of the Spy camera Devices when placed in a real-world lab setup where there are multiple interferences at locations 1-5 (from left to right).**



(a) Algorithm comparison.

(b) Effect of time offset.

(c) Across different devices.

**Figure 9: CDF of AoA estimation error for (a) algorithm comparison, (b) time-offset-based noise decorrelation, and (c) heterogeneous spy-camera devices.**

- We compare the AoA estimation accuracy across different algorithms, including traditional MUSIC, SpotFi, and our proposed approach.
- We investigate the impact of time-offset-based noise decorrelation technique on system performance.
- We examine the generalization capability across heterogeneous spy-camera devices to demonstrate the robustness and practicality of our system.

**Result:** Fig. 9(a) presents the CDF of the AoA error for SpyDir, SpotFi, and MUSIC. SpyDir achieves an average error of only  $6.30^\circ$ , substantially outperforming SpotFi ( $59.89^\circ$ ) and MUSIC ( $21.06^\circ$ ). This improvement stems from SpyDir’s sparse matrix optimization-based AoA solver, which remains stable even when the channel matrix is low rank—a regime where both SpotFi and MUSIC degrade sharply.

Fig. 9(b) evaluates SpyDir with and without applying the time-offset technique. Introducing the offset reduces the average error from  $63.43^\circ$  to  $6.30^\circ$ , demonstrating that it effectively decorrelates noise across switching-antenna ports and enables SpyDir to extract fine-grained AoA cues from extremely weak emanation signals.

Fig. 9(c) reports AoA accuracy across different spy-camera devices. The error remains consistently low regardless of device model, indicating that SpyDir is hardware-agnostic and generalizes across heterogeneous IoT camera platforms. Because SpyDir relies only on the emanation structure rather

than device-specific features, it scales naturally to diverse real-world spy camera deployments.

**Remark:** The above results demonstrate that SpyDir reliably delivers accurate AoA estimation for spy-camera emanations even in multipath-rich indoor environments. This performance arises from three key technical contributions: (1) sparse matrix optimization for robust AoA derivation, (2) non-coherent temporal averaging to enhance weak emanations, and (3) time-offset-based noise decorrelation across switching antennas. Importantly, SpyDir requires only the periodicity of the emanation signal and imposes no assumptions on its waveform, enabling broad applicability for hidden-camera detection. We believe this work advances emanation-based source localization and represents a step toward practical, privacy-preserving defense against covert surveillance.

### 6.3 Microbenchmarks

**6.3.1 Impact of Range.** The distance between the spy camera and SpyDir affects the received leakage strength and, consequently, the AoA estimation accuracy.

**Method:** We place the spy camera at varying distances from SpyDir in a real indoor environment and measure the resulting AoA estimation error.

**Result:** Fig. 10 reports the mean and standard deviation of AoA error across distances. AoA accuracy remains stable up to approximately 200 cm, beyond which the error increases

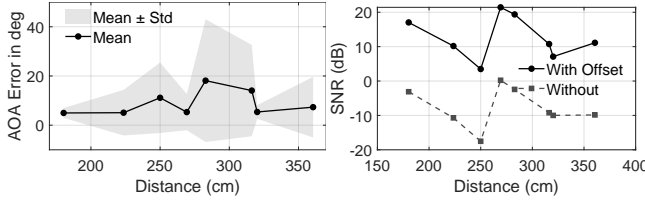


**Figure 10: AoA estimation error over different distances between the spy device and SpyDir.**

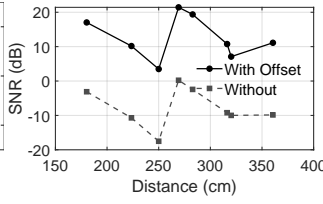


**Figure 11: SNR of the sniffed emanations over different distances with and without time offset.**

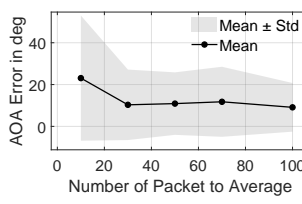


**Figure 12: AoA estimation error over different numbers of averaging packets. Each packet last for 50ms.**

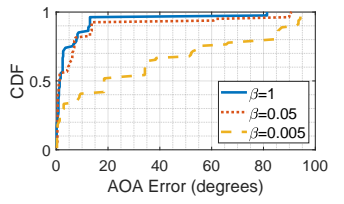


**Figure 13: CDF of AoA estimation error for various value of  $\beta$  (super parameter in Equation 13).**

sharply (e.g., at 225 cm), revealing SpyDir’s practical operating range. This degradation stems from reduced leakage strength and a stronger influence of multipath at low SNRs. Within the 200 cm range, however, SpyDir remains robust and maintains consistently low AoA error, since we enhance the emanation SNR through time-offset compensation.

**6.3.2 Impact of Time Offset.** SpyDir uses non-coherent averaging across packets, which benefits from noise decorrelation achieved via our time-offset mechanism.

**Method:** We compute the relative SNR (emanation spike amplitude over noise floor) at various distances, comparing measurements with and without the time offset.

**Result.** As shown in Fig. 11, the time offset provides a dramatic and consistent SNR improvement across all distances. Without the offset, SNR falls from 10 dB to below -10 dB, making the leakage nearly undetectable. With the offset, SNR remains above 20 dB at short distances and above 10 dB at the farthest point, offering a **10–25 dB gain**. This large improvement arises from noise decorrelation across the switched antenna ports, enabling non-coherent averaging to effectively enhance the periodic leakage while suppressing noise. Consequently, SpyDir maintains usable SNR for AoA estimation at significantly longer ranges.

**6.3.3 Impact of Time-Averaging Window Length.** Because leakage signals are extremely weak, increasing the averaging window substantially improves AoA accuracy. We employ non-coherent averaging to strengthen the periodic leakage component while suppressing unstructured noise and evaluate its effect on AoA performance.

**Method:** We vary the number of averaged packets (each packet is 50 ms) to study how strengthening the leakage signal affects AoA accuracy. For each window size, we average the IQ samples and extract the leakage spikes. The structured, periodic nature of clock leakage persists across packets, whereas noise averages out, making non-coherent averaging effective.

**Result.** Fig. 12 shows that both the mean and standard deviation of AoA error decrease as more packets are averaged.

Averaging 100 packets reduces the AoA error by 13.9° and lowers the standard deviation by 60% compared to averaging 10 packets. This improvement arises because the periodic leakage reinforces across packets, whereas unstructured noise is suppressed by averaging. The stronger reconstructed leakage then leads to significantly more accurate AoA estimation.

**6.3.4 Impact of  $\beta$ .** During the experiment, we observed that SpyDir’s AoA estimation relies on a sparsity-regularized optimization (Eq. 13), where the hyperparameter  $\beta$  controls the sparsity level.

**Method.** Using controlled simulations of multipath-rich indoor environments, we vary  $\beta$  and measure the resulting AoA estimation error. We then apply the empirically optimal value  $\beta = 1$  in real experiments.

**Result.** Fig. 13 shows the CDF of AoA estimation error for different values of  $\beta$ . The choice of  $\beta$  directly controls the sparsity of the recovered AoA profile, and thus overly small or overly large values degrade accuracy. When  $\beta$  is too small (e.g.,  $\beta = 0.005$ ), the solution becomes insufficiently regularized, allowing noise to introduce many spurious AoA components and leading to large errors. Conversely, when  $\beta$  is too large, the optimization becomes over-sparse and suppresses valid paths, causing the estimated channel to collapse toward zero.

Across the tested values,  $\beta = 1$  provides the best balance between sparsity and fidelity, resulting in the lowest AoA estimation error. Therefore, SpyDir adopts  $\beta = 1$  as the empirically optimal value for all deployments.

## 7 Related Work

**Dedicated detectors.** A straightforward way to detect hidden IoT devices is to use dedicated detectors [1, 2, 26, 29], which require users to manually sweep the detector around the environment. These devices sense harmonics generated by electronic components through near-field coupling between the detector and the device’s circuitry. As a result, they impose substantial human effort and cannot support automated or fine-grained localization. In contrast, SpyDir

performs automated detection and localization using emanations passively emitted by powered-on IoT devices, without requiring any active transmission or handheld scanning.

**Camera and laser sensor-based detection.** Hidden cameras pose a significant privacy threat, and many prior approaches detect them using optical sensors such as cameras or lasers [10, 14, 18–20, 28, 31, 33, 41, 46]. These methods exploit visible hardware features such as lens reflections or LED indicators to identify or localize cameras. However, such approaches depend on line-of-sight visibility and on the presence of detectable optical components, making them ineffective when devices are concealed behind objects, embedded in furniture, or otherwise visually obscured.

**Traffic-based detection.** Hidden IoT devices equipped with radio transceivers often generate wireless traffic, enabling a variety of traffic-analysis-based detection approaches [4, 5, 11, 13, 15, 21, 24, 25, 32, 36, 38, 42]. For example, MotionCompass [11] detects hidden cameras by correlating their transmitted traffic with a user’s motion trajectory. However, such approaches provide only coarse-grained localization and require carefully planned user movement. In contrast, SpyDir does not rely on wireless traffic at all; it operates solely on unintentional electromagnetic emanations and can detect and localize spy devices even when they are not actively transmitting.

**Emanation-based detection.** Recent work leverages unintentional electromagnetic emanations to detect hidden IoT devices in indoor environments, since such emanations are produced automatically by virtually all electronic devices [16, 22, 37, 40, 48]. For example, RFScan [40] detects hidden devices by scanning for their emanation harmonics and attempts localization using a directional antenna. However, its accuracy degrades severely indoors because the method depends heavily on received signal strength and is highly susceptible to multipath effects. Similarly, ESauron [45] relies on the RSSI of electromagnetic radiation for detection but faces analogous challenges under complex propagation conditions. Although CamFirm [17] advances the state of the art by actively modulating ambient brightness to elicit camera-specific radiation for localization, its operation is confined to dim environments and does not generalize to typical indoor settings. More critically, all these approaches follow a search-based paradigm—requiring physical movement within the environment and offering only coarse-grained location estimates—which fundamentally restricts their real-world utility. More broadly, most emanation-based systems focus solely on detection and do not provide precise localization of the hidden cameras. In contrast, SpyDir addresses this gap by using a custom switched-antenna array and a novel optimization-based AoA estimator that enables accurate localization directly from emanations

**AoA estimation.** AoA estimation has been extensively studied in indoor wireless localization, with techniques through antenna array ranging from geometry-based methods [6] and FFT-based estimators [35] to subspace methods such as MUSIC [9] and hybrid approaches like SpotFi [12]. However, these methods assume access to actively transmitted signals with known pilots or high-quality CSI, conditions that do not hold for unintentional emanations. In SpyDir’s task, the emanations are extremely weak and produce a low-rank relative channel matrix, making traditional AoA techniques ineffective. To overcome these limitations, SpyDir introduces a sparse optimization-based AoA estimator specifically designed for weak, pilotless emanations captured via a switched-antenna array.

## 8 Discussion

**Practical Insights and System Behavior.** SpyDir focuses on the problem of localizing hidden spy devices using their unintentional electromagnetic emanations. While SpyDir benefits from existing emanation-detection techniques, the design of robust detection algorithms is outside the scope of this work. Prior efforts [16, 40, 48] provide effective methods for identifying weak leakage signatures, and SpyDir can operate in conjunction with any such detector.

A key contribution of SpyDir is its ability to extend the practical detection range up to 200cm, a 120% improvement over state-of-the-art approaches. More importantly, SpyDir achieves accurate direction finding from weak, pilotless emanations, with a median AoA error of  $4.87^\circ$  and a 90th-percentile error of  $15.08^\circ$ . This demonstrates that accurate localization of devices emitting extremely low-power leakage is feasible even in multipath-rich indoor environments.

**Limitations and Future Work** Although SpyDir tolerates interference from other IoT devices, it still depends on the underlying detector to identify the correct emanation frequency of a target device. Existing detectors focus mainly on clock-based leakage from hidden cameras, and extending this capability to a broader set of IoT devices (e.g., microphones with significantly weaker leakage) remains an open challenge. A systematic characterization of leakage frequencies across different commercial devices, especially the weaker leakage from microphones, would further improve the robustness of emanation-based localization.

In addition, the wideband nature of sub-GHz leakage requires a relatively large antenna aperture to achieve sufficient angular resolution. This introduces a physical footprint that is limited by the capabilities of commodity SDR hardware. Future work will explore (i) antenna-placement strategies that emulate larger apertures in compact form factors [47], and (ii) detection and utilization of higher-frequency leakage components, which would naturally support smaller array geometries.

## References

- [1] Amazon. 2023. JMDHKK Anti Spy Detector, Bug Detector, Hidden Camera Detectors, GPS Detector, RF Signal Scanner Device Detector for GPS Tracker Listening Device Camera Finder. <https://a.co/d/17o2DyG>.
- [2] Amazon. 2023. Knight 5-in-1 Hidden Devices Detector Hidden Camera Detectors GPS, RF Detector Bug Detector Anti Spy Detector Hidden Camera Finder GPS Radio Frequency Detector de camaras y microfonos ocultos. <https://a.co/d/3onwqGh>.
- [3] Roshan Ayyalasomayajula, Aditya Arun, Chenfeng Wu, Sanatan Sharma, Abhishek Rajkumar Sethi, Deepak Vasishth, and Dinesh Bharadia. 2020. Deep learning based wireless localization for indoor navigation. In *Proceedings of the 26th Annual International Conference on Mobile Computing and Networking*. 1–14.
- [4] Yushi Cheng, Xiaoyu Ji, Tianyang Lu, and Wenyuan Xu. 2018. Dewicam: Detecting hidden wireless cameras via smartphones. In *Proceedings of the 2018 on Asia Conference on Computer and Communications Security*. ACM, none, 1–13.
- [5] Yushi Cheng, Xiaoyu Ji, Tianyang Lu, and Wenyuan Xu. 2019. On detecting hidden wireless cameras: A traffic pattern-based approach. *IEEE Transactions on Mobile Computing* 19, 4 (2019), 907–921.
- [6] Sheng-Fu Chuang, Wen-Rong Wu, and Yen-Ting Liu. 2015. High-resolution AoA estimation for hybrid antenna arrays. *IEEE Transactions on Antennas and Propagation* 63, 7 (2015), 2955–2968.
- [7] cnn. 2024. Takeaways from CNN’s Investigation: How Airbnb fails to protect its guests from hidden cameras. <https://www.cnn.com/2024/07/10/business/airbnb-hidden-cameras-key-takeaways-invs/index.html>.
- [8] M5 Docs. 2025. TimerCamera X. [https://docs.m5stack.com/en/unit/timercam\\_x](https://docs.m5stack.com/en/unit/timercam_x).
- [9] Benjamin Friedlander. 1990. A sensitivity analysis of the MUSIC algorithm. *IEEE Transactions on acoustics, speech, and signal processing* 38, 10 (1990), 1740–1751.
- [10] Sifeng He, Yuan Meng, and Mali Gong. 2018. Active laser detection system for recognizing surveillance devices. *Optics Communications* 426 (2018), 313–324.
- [11] Yan He, Qiuye He, Song Fang, and Yao Liu. 2021. MotionCompass: pinpointing wireless camera via motion-activated traffic. In *Proceedings of the 19th Annual International Conference on Mobile Systems, Applications, and Services*. ACM, none, 215–227.
- [12] Manikanta Kotaru, Kiran Joshi, Dinesh Bharadia, and Sachin Katti. 2015. Spotfi: Decimeter level localization using wifi. In *Proceedings of the 2015 ACM conference on special interest group on data communication*. 269–282.
- [13] Brent Lagesse, Kevin Wu, Jaynie Shorb, and Zealous Zhu. 2018. Automated Hidden Sensor Detection in Sensor-Rich Spaces. In *2018 IEEE International Conference on Pervasive Computing and Communications Workshops (PerCom Workshops)*. IEEE, none, none, 433–435.
- [14] Li Li, Jianlin Ren, and Xingbin Wang. 2015. Fast cat-eye effect target recognition based on saliency extraction. *Optics Communications* 350 (2015), 33–39.
- [15] Zhijing Li, Zhujun Xiao, Yanzi Zhu, Irene Pattarachanyakul, Ben Y Zhao, and Haitao Zheng. 2018. Adversarial localization against wireless cameras. In *Proceedings of the 19th International Workshop on Mobile Computing Systems & Applications*. none, none, 87–92.
- [16] Zhengxiong Li, Zhuolin Yang, Chen Song, Changzhi Li, Zhengyu Peng, and Wenyao Xu. 2018. E-eye: Hidden electronics recognition through mmwave nonlinear effects. In *Proceedings of the 16th ACM Conference on Embedded Networked Sensor Systems*. none, none, 68–81.
- [17] Qianru Liao, Jinyu Lin, Yongzhi Huang, Zijun Gong, and Kaishun Wu. 2025. CamFirm: A Compact FM-Based Module for Hidden Camera Detection. In *2025 IEEE International Conference on Pervasive Computing and Communications (PerCom)*. IEEE, 57–66.
- [18] Chun Liu, Changming Zhao, Haiyang Zhang, Zilong Zhang, Zitao Cai, and Zhipeng Li. 2019. Spectrum classification using convolutional neural networks for a mini-camera detection system. *Applied optics* 58, 33 (2019), 9230–9239.
- [19] Chun Liu, Changming Zhao, Haiyang Zhang, Zilong Zhang, Shuyuan Gao, and Yunshi Wang. 2019. Analysis of mini-camera’s cat-eye retro-reflection for characterization of diffraction rings and arrayed spots. *IEEE Photonics Journal* 11, 4 (2019), 1–12.
- [20] Chun Liu, Changming Zhao, Haiyang Zhang, Zilong Zhang, Yanwang Zhai, and Yali Zhang. 2019. Design of an active laser mini-camera detection system using cnn. *IEEE Photonics Journal* 11, 6 (2019), 1–12.
- [21] Tian Liu, Ziyu Liu, Jun Huang, Rui Tan, and Zhen Tan. 2018. Detecting wireless spy cameras via stimulating and probing. In *Proceedings of the 16th Annual International Conference on Mobile Systems, Applications, and Services*. none, none, 243–255.
- [22] Ziwei Liu, Feng Lin, Chao Wang, Yijie Shen, Zhongjie Ba, Li Lu, Wenyao Xu, and Kui Ren. 2023. CamRadar: Hidden Camera Detection Leveraging Amplitude-modulated Sensor Images Embedded in Electromagnetic Emanations. *Proceedings of the ACM on Interactive, Mobile, Wearable and Ubiquitous Technologies* 6, 4 (2023), 1–25.
- [23] Zhongqiang Luo, Chengjie Li, and Lidong Zhu. 2018. A comprehensive survey on blind source separation for wireless adaptive processing: Principles, perspectives, challenges and new research directions. *Ieee Access* 6 (2018), 66685–66708.
- [24] Markus Miettinen, Samuel Marchal, Ibbad Hafeez, N Asokan, Ahmad-Reza Sadeghi, and Sasu Tarkoma. 2017. Iot sentinel: Automated device-type identification for security enforcement in iot. In *2017 IEEE 37th International Conference on Distributed Computing Systems (ICDCS)*. IEEE, none, none, 2177–2184.
- [25] Richard Mitev, Anna Pazii, Markus Miettinen, William Enck, and Ahmad-Reza Sadeghi. 2020. Leakypick: Iot audio spy detector. In *Annual Computer Security Applications Conference*. none, none, 694–705.
- [26] online source. 2023. Dedicated detectors. <https://www.spygadgets.com/collections/counter-surveillance>.
- [27] pSemi Corporation. 2021. PE42582 UltraCMOS SP8T RF Switch Data Sheet. <https://www.psemi.com/pdf/datasheets/pe42582ds.pdf>. Product specification, DOC-76247-4 (03/2021).
- [28] Feng Qian, Bao Zhang, Chuanli Yin, Mingyu Yang, and Xiantao Li. 2015. Recognition of interior photoelectric devices by using dual criteria of shape and local texture. *Optical Engineering* 54, 12 (2015), 123110–123110.
- [29] REI. 2023. Dedicated detectors. <https://reiusa.net/nljd/orion-hx-deluxe-nljd/>.
- [30] DF Robot. 2025. ESP32 CAM Development Board. [https://media.digikey.com/pdf/Data%20Sheets/DFRobot%20PDFs/DFR0602\\_Web.pdf](https://media.digikey.com/pdf/Data%20Sheets/DFRobot%20PDFs/DFR0602_Web.pdf).
- [31] Laurel Sadler and Troy A Alexander. 2010. Mobile optical detection system for counter-surveillance. In *Ground/Air Multi-Sensor Interoperability, Integration, and Networking for Persistent ISR*, Vol. 7694. SPIE, none, none, 227–234.
- [32] Muhammad Salman, Nguyen Dao, Uichin Lee, and Youngtae Noh. 2022. CSI: DeSpy: Enabling Effortless Spy Camera Detection via Passive Sensing of User Activities and Bitrate Variations. *Proceedings of the ACM on Interactive, Mobile, Wearable and Ubiquitous Technologies* 6, 2 (2022), 1–27.
- [33] Sriram Sami, Sean Rui Xiang Tan, Bangjie Sun, and Jun Han. 2021. LAPD: Hidden Spy Camera Detection using Smartphone Time-of-Flight Sensors. In *Proceedings of the 19th ACM Conference on Embedded Networked Sensor Systems*. none, none, 288–301.

- [34] Ralph Schmidt. 1986. Multiple emitter location and signal parameter estimation. *IEEE transactions on antennas and propagation* 34, 3 (1986), 276–280.
- [35] KP Schwarz, MG Sideris, and R Forsberg. 1990. The use of FFT techniques in physical geodesy. *Geophysical Journal International* 100, 3 (1990), 485–514.
- [36] Rahul Anand Sharma, Elahe Soltanaghaei, Anthony Rowe, and Vyasa Sekar. 2022. Lumos: Identifying and localizing diverse hidden {IoT} devices in an unfamiliar environment. In *31st USENIX Security Symposium (USENIX Security 22)*. none, none, 1095–1112.
- [37] Cheng Shen and Jun Huang. 2021. {EarFisher}: Detecting Wireless Eavesdroppers by Stimulating and Sensing Memory {EMR}. In *18th USENIX Symposium on Networked Systems Design and Implementation (NSDI 21)*. none, none, 873–886.
- [38] Akash Deep Singh, Luis Garcia, Joseph Noor, and Mani B Srivastava. 2021. I Always Feel Like Somebody’s Sensing Me! A Framework to Detect, Identify, and Localize Clandestine Wireless Sensors.. In *USENIX Security Symposium*. none, none, 1829–1846.
- [39] Chandra Steele. 2024. Does Your Airbnb Have Hidden Cameras? Here’s How to Check. <https://www.pcmag.com/how-to/how-to-check-for-hidden-cameras-airbnb-vacation-rental>.
- [40] Wei Sun, Hadi Givehchian, and Dinesh Bharadia. 2025. Revealing Hidden IoT Devices through Passive Detection, Fingerprinting, and Localization. *Proceedings on Privacy Enhancing Technologies* (2025).
- [41] Daniel Svedbrand, Lars Allard, Magnus Pettersson, Pontus Köhler, Markus Henriksson, and Lars Sjökvist. 2019. Optics detection using an avalanche photo diode array and the scanning-slit-method. In *Technologies for Optical Countermeasures XVI*, Vol. 11161. SPIE, none, none, 167–177.
- [42] Kevin Wu and Brent Lagesse. 2019. Do you see what i see?< subtitle> detecting hidden streaming cameras through similarity of simultaneous observation. In *2019 IEEE International Conference on Pervasive Computing and Communications (PerCom)*. IEEE, none, none, 1–10.
- [43] Nabil R Yousef, Ali H Sayed, and Louay MA Jalloul. 2003. Robust wireless location over fading channels. *IEEE transactions on vehicular technology* 52, 1 (2003), 117–126.
- [44] Chengpu Yu, Lihua Xie, and Yeng Chai Soh. 2014. Blind channel and source estimation in networked systems. *IEEE Transactions on Signal Processing* 62, 17 (2014), 4611–4626.
- [45] Qibo Zhang, Daibo Liu, Xinyu Zhang, Zhichao Cao, Fanzi Zeng, Hongbo Jiang, and Wenqiang Jin. 2024. Eye of Sauron: {Long-Range} Hidden Spy Camera Detection and Positioning with Inbuilt Memory {EM} Radiation. In *33rd USENIX Security Symposium (USENIX Security 24)*. 109–126.
- [46] X Zhang and Feng Qian. 2017. A Fast Recognition Algorithm for Photoelectric Peeping Equipment. *DEStech Transactions on Computer Science and Engineering* none (2017), none.
- [47] Wang Zheng, Xiaofei Zhang, Yunfei Wang, Mengjie Zhou, and Qihui Wu. 2019. Extended coprime array configuration generating large-scale antenna co-array in massive MIMO system. *IEEE Transactions on Vehicular Technology* 68, 8 (2019), 7841–7853.
- [48] Ruochoen Zhou, Xiaoyu Ji, Chen Yan, Yi-Chao Chen, Wenyan Xu, and Chaohao Li. 2023. Dehirec: Detecting hidden voice recorders via adc electromagnetic radiation. In *2023 IEEE Symposium on Security and Privacy (SP)*. IEEE, 3113–3128.
- [49] Agustin Zuniga, Naser Hossein Motlagh, Mohammad A Hoque, Sasu Tarkoma, Huber Flores, and Petteri Nurmi. 2022. See no evil: Discovering covert surveillance devices using thermal imaging. *IEEE Pervasive Computing* 21, 4 (2022), 33–42.